research papers

Texture analysis from synchrotron diffraction images with the Rietveld method: dinosaur tendon and salmon scale

Ivan Lonardelli,[a,b] Hans-Rudolf Wenk,[a]* Luca Lutterotti[a,b] and Mark Goodwin[c]

[a]Department of Earth and Planetary Science, University of California, Berkeley, CA 94720, USA,
[b]Dipartimento Ingegneria dei Materiali e Tecnologie Industriali, Università Trento, Italy, and
[c]Museum of Paleontology, University of California, Berkeley, CA 94720, USA.
E-mail: wenk@seismo.berkeley.edu

A Rietveld method is described which extracts information on crystal structure, texture and microstructure directly from two-dimensional synchrotron diffraction images. This is advantageous over conventional texture analysis that relies on individual diffraction peaks, particularly for low-symmetry materials with many overlapping peaks and images with a poor peak-to-background ratio. The method is applied to two mineralized biological samples with hydroxylapatite fabrics: an ossified pachycephalosaurid dinosaur tendon and an Atlantic salmon scale. Both are measured using monochromatic synchrotron X-rays. The dinosaur tendon has very strongly oriented crystals with c-axes parallel to the tendon direction. The salmon scale displays a weak texture.

Keywords: texture analysis; Rietveld method; biomineralization; dinosaur tendon; salmon scale; hydroxylapatite.

1. Introduction

In many biomineralized materials, the crystallites are strongly aligned by characteristic patterns that influence their macroscopic mechanical properties. Surprisingly, relatively little is known about quantitative orientation characteristics. This is due, in part, to the extreme heterogeneity and poor crystallinity of bioapatite resulting in diffuse diffraction patterns with many overlapping peaks. In a previous investigation, Wenk & Heidelbach (1998) applied microbeam synchrotron radiation for quantitative texture analysis of a bovine bone and turkey tendon. This procedure relied on extracting diffraction intensities from individual diffraction peaks, performing the texture analysis based on variations of intensities along Debye rings (Heidelbach et al., 1999; Wenk & Grigull, 2003), and was extremely time-consuming. Furthermore, this method is only applicable if peaks are well separated and the background is well defined, which is rarely the case.

In the images of a dinosaur tendon (Fig. 1a) and particularly in a salmon scale (Fig. 1b), diffractions from hydroxylapatite are weak, barely above background with many superposed peaks. This was a major incentive for developing a new technique for texture analysis based on the Rietveld method that relies on simultaneous full two-dimensional image analysis.

Previously, the Rietveld method (Rietveld, 1969) was used for texture analysis of time-of-flight neutron diffraction data and implemented in the software package *MAUD* (Lutterotti et al., 1997). The method has been successful in analyzing low-symmetry compounds (Xie et al., 2003) and composites (Chateigner et al., 1998). In the case of neutron diffraction, one-dimensional diffraction spectra measured in different sample orientations are combined. For synchrotron data, the challenge is the use of whole two-dimensional images as input without preliminary data processing, e.g. in *FIT2D* (Hammersley, 1997).

In this communication we are emphasizing methodological issues. The biological significance will be discussed elsewhere.
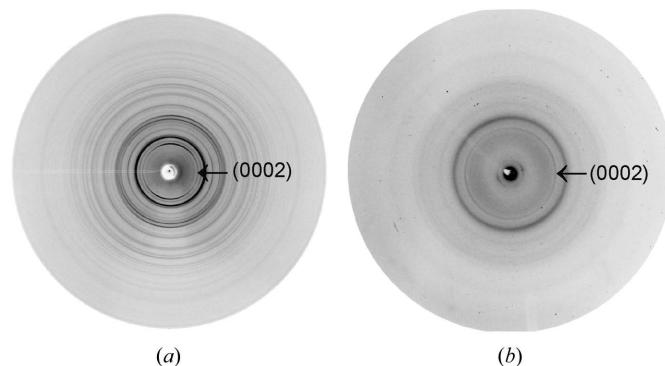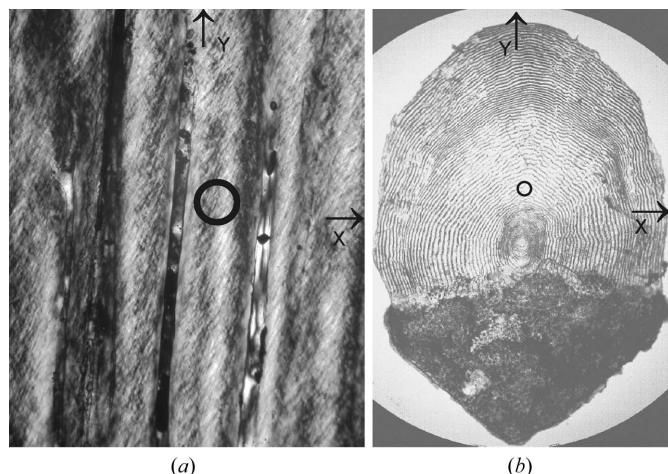

Figure 1
Two-dimensional synchrotron diffraction images as they were used in the Rietveld analysis. (a) Dinosaur tendon recorded using an image plate. (b) Salmon scale recorded using a CCD camera. The (0002) Debye rings show strong intensity variation for dinosaur and a lesser one for salmon scale. These variations are indicative of texture.

2. Materials and experiments

We report here the results for texture analysis in two biological samples. The first is an ossified pachycephalosaurid dinosaur tendon (University of California Museum of Paleontology, Berkeley, UCMP 128383) from an associated skeleton of *Stygimoloch spinifer* found in the Late Cretaceous Hell Creek Formation (*ca* 68 M.a.) of Garfield County, Montana (Goodwin *et al.*, 1998). Many dinosaurs have very well developed ossified tendons in their tail region that provide additional stiffness for counter balance (Curry, 2002). Despite its antiquity, UCMP 128383 still possesses an original hydroxylapatite fabric, though this may have been modified by *post mortem* ionic exchange and diagenesis (Kolodny *et al.*, 1996). Preliminary examination using a petrographic microscope reveals strong preferred orientation (Fig. 2a). The texture is locally heterogeneous and a focused synchrotron beam was necessary to select a relatively homogeneous area of interest. The second sample is a scale from an Atlantic salmon, *Salmo salar* L, provided by Dr Philip Bacon (Center for Ecology and Hydrology, Banchory, Scotland). The salmon scale displays growth rings (Fig. 2b). By scanning across the sample we observed that texture variability within these growth rings is minimal and we focused on characterizing the texture pattern at a single spot in the scale.

The general diffraction geometry is straightforward (see Fig. 3a). A beam is focused on the sample that is mounted on a glass needle. In the examples considered here, the sample is a thin slice, larger than the beam diameter. In texture analysis the orientation is of crucial importance. We place a Cartesian coordinate system XYZ in the sample (Fig. 2, Z is perpendicular to the flat specimen, Y is the needle axis) and later relate orientation information to that system. On a goniometer the sample can be rotated around a perpendicular axis. In the initial setting the surface normal Z is parallel to the incident beam. Then the flat sample is tilted around the needle axis Y

by an angle ω. Transmission diffraction patterns are recorded using a flat CCD camera or image-plate detector, mounted perpendicular to the incident beam behind the sample. In our convention each Debye ring (with opening angle 4θ) corresponds to a small circle on the pole sphere (with a radius or 'pole distance' $90° - \theta$). The angle η on the Debye ring corresponds to the pole sphere azimuth, when viewed along the incident X-ray. Because of centrosymmetry there is an equivalent small circle on the opposite hemisphere. If we view the pole sphere along the tilt axis Y (which is achieved by a sample rotation $\chi = 90°$ in the *MAUD* program, see Appendix A), the small circles on the pole figure appear as a pair of lines separated by a distance 2θ (Fig. 3b). They are drawn schematically as a pair of parallel straight lines. In reality they are curved in equal area projection. Intensity variations along the Debye ring are directly proportional to pole densities. For a sample at normal incidence ($\omega = 0°$) the pair of lines are horizontal in the pole figure. Tilting the sample by ω rotates the lines on the pole figure by the same angle. Images with different sample tilts are combined to increase pole figure coverage.
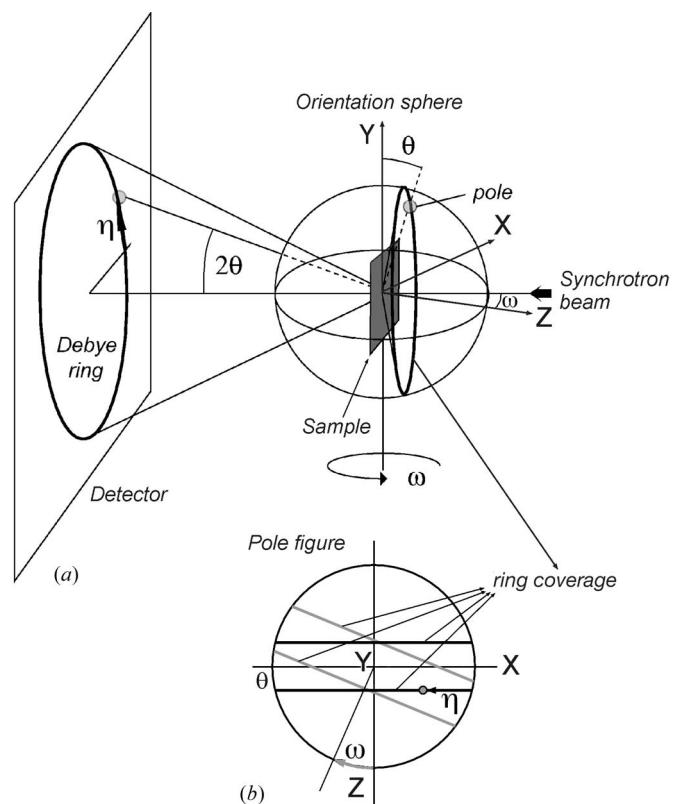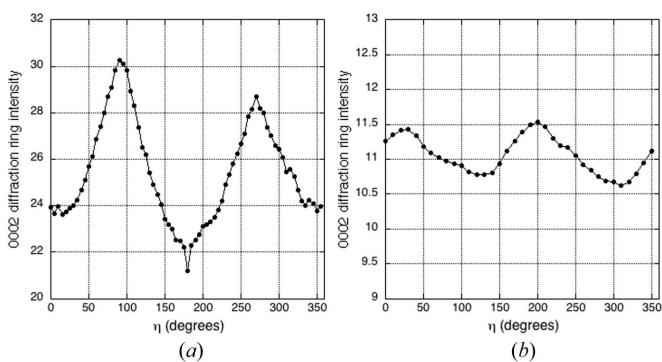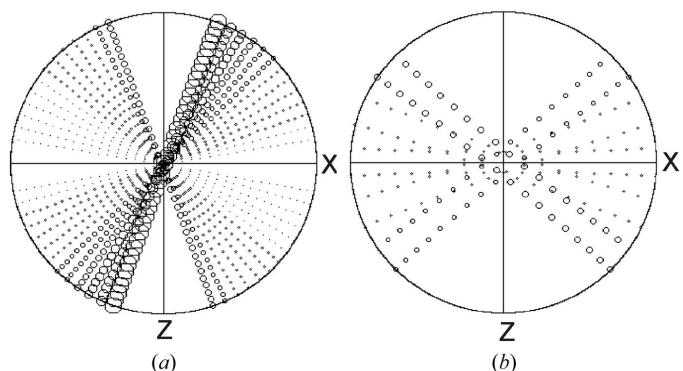

Figure 3
(*a*) Diffraction geometry of a synchrotron experiment in transmission; the samples are rotated around the Y axis (ω rotation) for better pole figure coverage. The scattering vector for each Debye ring produces a small circle on the orientation sphere in (*a*). In the corresponding pole figure (*b*), we are looking at the projection of this small circle along the Y axis (from top). The small circle in this projection appears as a pair of lines that are drawn schematically as parallel straight lines. For tilted orientations the lines are rotated around the pole figure center by ω. The indicated 'pole' in (*a*) corresponds to the scattering vector for a specific Debye ring diffracted at a 2θ angle and at an angle η along the ring.

Figure 2
Photomicrograph of (*a*) a thin section of dinosaur tendon (UCMP 128383) showing well organized longitudinal Haversian canals, and (*b*) Atlantic salmon scale. Image dimensions are 1 mm across for the dinosaur tendon, and 4 mm for the salmon scale. The sample coordinate system (*XYZ*) used in this study is indicated. The circle indicates the location of the texture analysis.

The dinosaur tendon was measured at APS (Advanced Photon Source) at Argonne National Laboratory, on high-energy beamline 11-ID with a wavelength of 0.146 Å (85 keV), beam diameter 50 µm and a simple goniometer. A section was prepared parallel to the long axis of the tendon, and a flat sample, 30 µm in thickness and 100 µm × 100 µm in extent, was used for the analysis. Images were recorded using a 3450 × 3450 image-plate detector, mounted orthogonal to the beam path. Intensity variations along Debye rings (Fig. 1a) immediately reveal the presence of texture. Fig. 4(a) shows a variation for the (0002) Debye ring intensity of over 20%. Images were recorded at 26 different ω tilt angles, rotating the sample around an axis perpendicular to the beam in 5° increments. The coverage is shown in Fig. 5(a), using 5° Debye-ring sectors.

The salmon scale was measured at ESRF (European Synchrotron Radiation Facility), at microfocus beamline ID13, with a wavelength of 0.7985 Å (15.6 keV) and a beam diameter of 5 µm. Images were recorded using a 1024 × 1024 CCD detector. Compared with the dinosaur tendon this sample was characterized by a smoother texture (see Fig. 1b).

Figure 4
(0002) Debye ring intensity variation (in arbitrary units) of (a) dinosaur tendon and (b) salmon scale. The dinosaur sample clearly shows a stronger texture than the salmon scale, confirmed in the analysis by the texture results.

Figure 5
Pole figures coverage for (a) dinosaur tendon and (b) salmon scale. Equal area projection. Debye rings have been integrated over 5° sectors for dinosaur tendon and 10° sectors for salmon scale. Coverage coming from the same image is visible in (a) by symbols with the same dimensions. The symbol size is proportional to the refined scale-factor/absorption-factor. For the dinosaur the pair of lines almost coincide because the θ angle (see Fig. 3b) is very low owing to high-energy radiation.

and fewer angular tilts were necessary to characterize the texture. Debye-ring intensity variations are less than 5% (Fig. 4b). The sample was tilted ten times in 10° ω increments to provide sufficient pole figure coverage (Fig. 5b). As a guideline, sharper textures require more data to be collected compared with smoother textures. In the extreme case of a random texture a single spectrum would be sufficient. Sharp textures require smaller cell grid sizes in order to take small angular texture variations into account.

In both cases an Al_2O_3 powder standard was used to calibrate the sample-to-detector distance and refine instrumental parameters.

3. Rietveld analysis from two-dimensional images

The image data were entered into the program *MAUD* (Materials Analysis Using Diffraction), a Rietveld code written in Java (Lutterotti *et al.*, 1997). The software has multiple applications for a wide range of materials and diffraction techniques. Instrument-specific parameters are required (*e.g.* for conventional X-rays, synchrotron X-rays, low-angle scattering, neutrons); phases need to be characterized (crystallography/structure, microstructure, texture, elastic strain); various diffraction data sets can be entered (including powder patterns, TOF neutron diffraction data in GSAS format, and now synchrotron images in ESRF and APS formats); and data sets from different instruments can be combined. Appendix *A* gives a brief summary of the *MAUD* procedure as applied to two-dimensional synchrotron images.

In this study, tiff images with 16 bit dynamic range are entered using an image manager. In a first approximation the image center can be found interactively on the monitor (this center is later refined in the Rietveld procedure). It is important that the pixel size is correct (in some *FIT2D* procedures this value is lost when tiff files are exported and needs to be re-entered manually). The user determines an inner and outer radius for integrations as well as the azimuthal range. The integrated slices are then used as spectral data for the Rietveld refinement. In our study the integration was performed over 5° sectors for the dinosaur sample and 10° sectors for the scale. For the dinosaur tendon, only a 180° sector of the image was used, while for the scale a full 360° sector, thus providing for both 36 spectra per image and coverages shown in Fig. 5.

Since the flat sample is tilted around axis ω (Fig. 3) relative to the beam, each image records a different sample volume (increasing with tilt angle) and with different absorption (Heidelbach *et al.*, 1999). This volume/absorption effect was accounted for by refining an image scale factor. Fig. 5 illustrates with symbol sizes that this scale factor is largest for high tilts. From the point of view of the analysis this scaling may present a problem since both the volume/absorption factor and possible sample heterogeneity in different volumes may affect texture results. However, such conceivable sample heterogeneities are more severe for conventional pole figure texture analysis, and less for the Rietveld method where possible variations are smoothed out by the use of multiple

Table 1
Lattice parameters and atomic positions compared with the starting structure for hydroxylapatite.

Standard deviations are shown in parentheses.

	a (Å)	c (Å)		Ca1	Ca2	P	O1	O2	O3	OH
Starting structure	9.418 (2)	6.875 (2)	x	2/3	−0.00657 (5)	0.36860 (6)	0.4850 (2)	0.4649 (2)	0.2580 (1)	0.0
(Hughes *et al.*, 1989)			y	1/3	0.24706 (5)	0.39866 (6)	0.3289 (2)	0.5871 (2)	0.3435 (1)	0.0
			z	0.00144 (8)	1/4	1/4	1/4	1/4	0.0703 (2)	0.1979 (6)
Dinosaur tendon	9.386 (1)	6.890 (1)	x	2/3	−0.0060 (3)	0.3668 (3)	0.5120 (6)	0.4671 (5)	0.2536 (4)	0.0
			y	1/3	0.2413 (2)	0.3945 (4)	0.3305 (6)	0.5707 (5)	0.3545 (3)	0.0
			z	0.0094 (4)	1/4	1/4	1/4	1/4	0.0709 (3)	0.22 (4)
Salmon scale	9.445 (9)	6.854 (3)		Owing to poor crystallinity the atomic positions were fixed						

reflections. It should be noted that not only texture but also the final structure is averaged over the experimentally sampled volume.
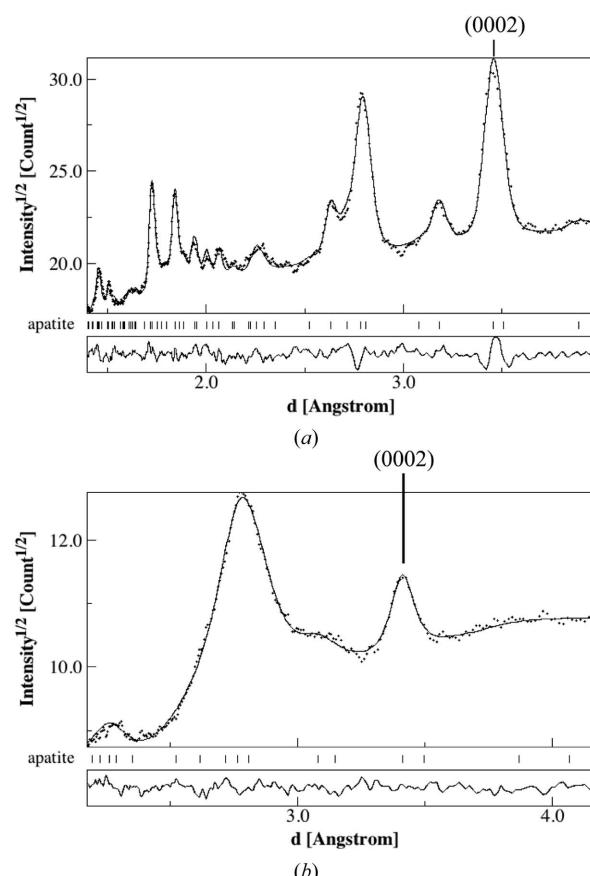
In the case of the dinosaur tendon, $26 \times 36 = 936$ spectra were used for the refinement. First, the instrument parameters, used to determine the center of the ring, were refined. Next, scale parameters (one for each image) and backgrounds (three for each spectrum) were refined. Crystallographic parameters [starting with the values of Hughes *et al.* (1989), for hydroxylapatite, space group $P6_3/m$] and crystallite size were refined in the following step. Anisotropic crystallite size was modelled using the Popa approach (Popa, 1998). Finally, the texture was refined using the tomographic *EWIMV* algorithm that is related to *WIMV* (Matthies & Vinel, 1982) and allows data to be entered at arbitrary positions. No sample symmetry was imposed. The refinement of the orientation distribution function (ODF) was carried out in a separate cycle, outside the Rietveld procedure. A 5° grid for the ODF and a 10° radius for the tube projection were used. Fig. 6(*a*) shows a typical spectrum and the fit. The agreement between observed and recalculated values is very good.

In the case of the salmon scale, $5 \times 36 = 180$ spectra were used and the refinement proceeded similar to the dinosaur tendon analysis. The spectrum in Fig. 6(*b*) shows much poorer crystallinity than the ossified tendon with broad peaks due to the small grain size. As a consequence, atomic positions were not refined in this case.

Figure 6
Typical diffraction spectrum for (*a*) dinosaur tendon and (*b*) salmon scale. Measured data (dots) and calculated Rietveld fit (solid line) are shown. Individual diffraction peaks are marked below the spectrum. The square root of the intensity is reported instead of the usual intensity to plot at iso-error and enhance the smaller peaks.

4. Results

4.1. Crystallographic parameters and crystallite size

With the Rietveld analysis, crystallographic parameters were refined and are listed in Table 1 and compared with the starting structure (Hughes *et al.*, 1989). Atomic coordinates with calculated standard deviation were refined for the dinosaur tendon. The poor crystallinity of both samples, particularly salmon scale, does not allow an accurate evaluation of the lattice parameters and atomic positions. Temperature factors for both samples were refined and kept equal for all atoms. Values are 0.27 for dinosaur tendon and 1.12 for salmon scale. The refined structure does not deviate much from values reported for other hydroxylapatite structures (Andreev, 1994;

Hughes *et al.*, 1989), including biological material (*e.g.* Wheeler & Leweis, 1977; Meneghini *et al.*, 2003).

The change of peak broadening with d was used to evaluate the crystallite size, defined as the size of a molecular well ordered domain that diffracts in phase. The mean size values evaluated from the line broadening of all *hkl* reflections inside the Rietveld are reported in Table 2. These values are considerably larger than those reported for mamillarian bones (*e.g.* Ziv & Weiner, 1993; Trueman *et al.*, 2004) and enamel (Elliott, 2002). It cannot be excluded that the reported high

Table 2
Refined crystallite sizes (in nm) of dinosaur tendon and salmon scale of some (hkl) reflections.

The values of standard deviations are from the Rietveld refinement.

hkil	0002	12$\bar{3}$1	21$\bar{3}$1	11$\bar{2}$2	31$\bar{4}$0
Dinosaur tendon	29.2 (8)	22.4 (8)	18.1 (8)	16.38 (8)	10.3 (3)
Salmon scale	16.5 (8)	7.2 (3)	5.2 (2)	4.7 (2)	6.6 (4)

Table 3
Quantitative texture information ODF and pole densities in multiples of a random distribution (m.r.d.) and width of main texture peak.

	Texture index (F2)	ODF (max–min)	(0001) (max–min)	(10$\bar{1}$0) (max–min)	(0001) FWHM
Dinosaur tendon	1.48	4.92–0.25	3.25–0.31	1.53–0.35	55°
Salmon scale	1.05	1.80–0.48	1.35–0.68	1.17–0.82	75°

Figure 7
(0001) and (10$\bar{1}$0) pole figures of (a) dinosaur tendon and (b) salmon scale. Equal area projection. The pole density scale in m.r.d. displays values of contours (linear scale). The coordinate system is indicated (compare with Fig. 2).

values are due to calibration problems, particularly the instrumental broadening function that was refined from an image of a standard sample (only a single parameter was refined for the peak width owing to the small 2θ range) and then held constant during the analysis of dinosaur tendon and salmon scale. The values are larger for tendon than for the scale, which is already qualitatively apparent in the diffraction images (Fig. 1). Crystallites are elongated along the c-axis, consistent with the observation of elongated platelets in bone material (e.g. Weiner & Price, 1986).

4.2. Texture

The results of the texture analysis for the two samples are summarized in Table 3. From the orientation distribution, pole figures (0001) and (10$\bar{1}$0) were calculated (Fig. 7) and are shown in the same orientation as the coverage (Fig. 5). In the dinosaur tendon, the texture is close to axially symmetric around the tendon direction (Y). The c-axes are preferentially aligned parallel to the tendon axis with a strong maximum of 3.25 m.r.d., in agreement with qualitative optical observations (Fig. 7a). The (10$\bar{1}$0) poles scatter more or less randomly around the c-axis (great circle in the XZ plane). The ODF minimum is 0.25 m.r.d. indicating that a substantial number of crystallites are randomly oriented. The width of the texture peak at half maximum is 55°. This is similar to texture documented for turkey tendon (Wenk & Heidelbach, 1998). The c-axis maximum of the turkey tendon was 6 m.r.d. and the width of the texture peak was 45°, slightly stronger than for the dinosaur.

When tendon is ossified into bone, a highly anisotropic material is produced. Anisotropy is maintained throughout secondary bone remodeling in extant cranes (Curry, 2002), turkeys (Bennett & Stafford, 1988) and, by inference, in dinosaurs. The tendons are not usually loaded significantly from side to side and maintain strength along their length. This is reflected by their Haversian systems that have their fibers
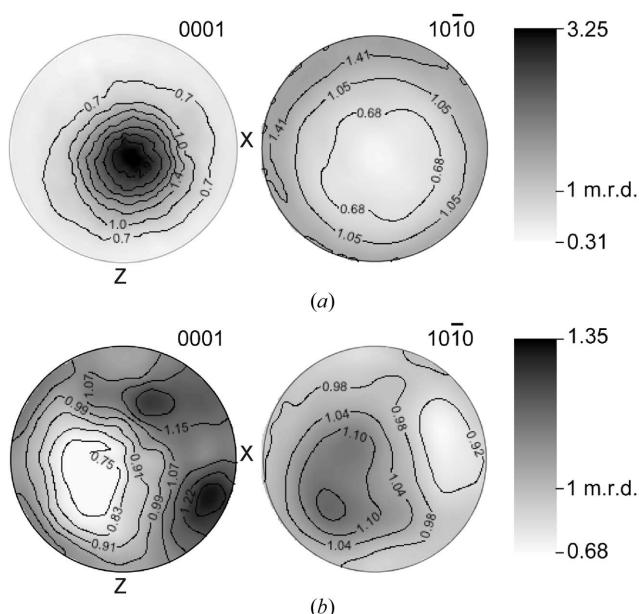
oriented almost all longitudinally (see Fig. 2a). The osteocyte lacunae are spindle-shaped and elongated in the same direction. This morphology is not typically observed in the lacunae of amniote osteocytes (Curry, 2002).

For the salmon scale the texture is weak and less regular, yet significant qualitatively as already visible on the Debye rings (Fig. 1b). The c-axes are aligned in two broad maxima, inclined symmetrically to the scale surface (which is perpendicular to Z in Fig. 7b). The c-axis minimum is in the scale surface. The ODF maximum is 1.35 m.r.d. and the minimum is 0.68 m.r.d., indicating that a large number of crystallites are oriented randomly. The width of the texture peak at half maximum for (0001) is 75°.

5. Conclusions

This note describes two new applications of synchrotron radiation to characterize crystallite orientation in highly heterogeneous biological apatite. A strong hydroxylapatite alignment was confirmed for the dinosaur tendon, a weak texture in the salmon scale. Because of their heterogeneity and weak scattering, these investigations could not have been undertaken using other techniques. With the methods established here, it is now possible to investigate texture variations between and within the bones and enamel of different species and tissue type (i.e. compact, cancellous, trabecular tissue).

The salmon scale shows a very weak but significant texture. The c-axes are aligned in maxima that are oblique to the surface of the scale. It was still possible to extract quantitative information about texture using the Rietveld method.

This study produced some new biological information on texture variations in calcified tissue, a field of great interest

(Kohn *et al.*, 2002). In this paper we emphasize a new development by applying the Rietveld technique to diffraction images to extract quantitative texture information. By using the Rietveld method and integrated image analysis, it is no longer necessary for texture analysis to rely on intensity variations on individual Debye rings, as was previously the case (*e.g.* Heidelbach *et al.*, 1999; Merkel *et al.*, 2002; Puig-Molina *et al.*, 2003; Wenk & Grigull, 2003). In our examples, using dinosaur tendon and a salmon scale, we document an application for analyzing complex images with weak diffraction and many overlapping peaks. A similar method was also successful in analyzing *in situ* high-pressure data obtained in diamond anvil cells, where the refinement of elastic strains and interpretation in terms of applied stresses are additional complications (Wenk *et al.*, 2004). In the future, it will be possible for synchrotron users to take texture into account in a systematic fashion. This is not only important for those interested in anisotropy but also for crystal structure investigations where texture information is a pre-requisite to weight intensities.

APPENDIX *A*
Summary of the *MAUD* Rietveld procedure for texture analysis of two-dimensional synchrotron images

(i) INSTRUMENT. In 'source', choose synchrotron model, enter the correct wavelength in 'options'. For 'angular calibration' select 'flat image transmission' and enter the sample/detector distance; other parameters that are subsequently refined are image center and tilting errors. For a correct calibration it is important to use first a standard sample with well defined lattice parameters, crystal structure and crystallite size and use the same procedure to refine detector distance, image center as well as instrumental aberration (Caglioti function) keeping crystallite sizes fixed and microstrains set to zero (under PHASES). The 2θ offset parameter should also be refined.

(ii) DATA. In 'data files', enter two-dimensional 16 bit tiff image using 'image manager' for importing area-detector data. When the image is loaded, choose from the plug-ins menu the 'multispectra from transmission image', set the correct parameters: sample/detector distance, center X, center Y, maximum radius for integration, starting and final azimuthal angle, number of spectra and tilt angle, to produce integrated spectra for angular slices.

(iii) PHASES. Enter crystallographic data from a structural database (*MAUD* can read structures in CIF format, the crystallographic information file format developed by IUCr) or input it by hand on the graphical interface. At the beginning select no texture (in 'advanced models'), and choose 'isotropic model' for microstructure parameters.

(iv) SAMPLE. In 'position', set φ, χ and $\omega = 0$ or choose a different angle if you want to change the sample reference axis. If $\chi = 0°$ then the pole figure is viewed along the incident-beam direction. In our case we entered $\chi = 90°$ to have the rotation (tilt) axis Y perpendicular to the pole figure plane.

The sample tilt angle ω has to be entered in 'data sets' for each spectrum/image individually.

(v) In 'data files', enable the spectra from only one two-dimensional image and refine the center of the image (under INSTRUMENT, angular calibration), background (at first only two parameters; this may be efficiently done interactively on the plot image to obtain an approximate solution) and intensity. Now we are ready to refine lattice parameters, structure and grain size for one image.

(vi) When these parameters are refined, we have a good starting point. Enable all spectra from all images and refine them simultaneously using all the previous-mentioned parameters.

(vii) To correct for volume and absorption with tilt, refine the function 'count/monitor' for each tilt angle (this can be done for all data files at once in the 'parameter list' frame).

(viii) Check pole figure coverage ('Graphics', 'Pole figure plot') to see whether your choice of angles is correct (compare it with an individual image!) and whether you have a good coverage of the pole figure. As a guideline, keep in mind that fewer diffraction peaks require a larger pole figure area to be covered and *vice versa*. Stronger textures require more data points per area. Smoother textures can be approached by a larger grid. Symmetries in the sample and crystal structure reduces the required coverage.

(ix) Now you are ready to refine all parameters and texture simultaneously. The E-WIMV method is preferred for quantitative texture analysis. Projection tube radius (*e.g.* 10°) and ODF resolution (*e.g.* 5°) depend on the sharpness of the texture and the available coverage. In the terminal output an indication of the ODF coverage from the experimental data is provided. If this is less than 100% you need more data or you need to enlarge the ODF resolution and/or tube projection parameter. To obtain more ODF details it is necessary to increase the measured data.

(x) View texture results in 'Graphics', 'Pole figures plot'. Compare calculated and experimental pole figures.

(xi) Review refined parameters and errors in the 'parameter list'.

(xii) Export the ODF, interpolated on a $5° \times 5° \times 5°$ grid, for further processing in *BEARTEX* (Wenk *et al.*, 1998), *e.g.* to smooth the ODF, calculate pole figures, transform coordinate systems and calculate polycrystalline physical properties.

References

Andreev, Y. G. (1994). *J. Appl. Cryst.* **27**, 288–297.
Bennett, M. B. & Stafford, J. A. (1988). *J. Zool.* **214**, 343–351.

Chateigner, D., Lutterotti, L. & Hansen, T. (1998). ILL Annual Report 97, pp. 28–29. ILL, Grenoble, France.

Curry, J. D. (2002). *Bones: Structure and Mechanics.* Princeton University Press.

Elliott, J. C. (2002). *Reviews in Mineralogy and Geochemistry*, Vol. 48, edited by M. J. Kohn, J. Ravokovan and J. M. Hughes, pp. 427–448. Washington, DC: Mineralogical Society of America.

Goodwin, M. B., Buchholtz, E. A. & Johnson, R. E. (1998). *J. Vertebr. Paleontol.* **18**, 363–375.

Hammersley, A. P. (1997). ESRF Internal Report ESRF97HA02T. ESRF, Grenoble, France.

Heidelbach, F., Riekel, C. & Wenk, H.-R. (1999). *J. Appl. Cryst.* **32**, 841–849.

Hughes, J. M., Cameron, M. & Crowley, K. D. (1989). *Am. Miner.* **74**, 870–876.

Kohn, M. J., Ravokan, J. & Hughes, J. M. (2002). *Reviews in Mineralogy and Geochemistry*, Vol. 48, edited by M. J. Kohn, J. Ravokovan and J. M. Hughes. Washington, DC: Mineralogical Society of America.

Kolodny, Y., Luz, B., Sander, M. & Clemens, W. A. (1996). *Paleogeogr. Paleaoclimat. Paleoecol.* **126**, 161–171.

Lutterotti, L., Matthies, S., Wenk, H.-R., Schultz, A. S. & Richardson, J. W. Jr (1997). *J. Appl. Phys.* **81**, 594–600.

Matthies, S. & Vinel, G. W. (1982). *Phys. Status Solidi B*, **112**, K111–K114.

Meneghini, C., Dalconi, M. C., Nuzzo, S., Mobilio, S. & Wenk, R. H. (2003). *Biophys. J.* **84**, 2021–2029.

Merkel, S., Wenk, H.-R., Shu, J., Shen, G., Gillet, P., Mao, H.-K. & Hemley, R. J. (2002). *J. Geophys. Res.* **107**, 2271–2288.

Popa, N. C. (1998). *J. Appl. Cryst.* **31**, 176–180.

Puig-Molina, A., Wenk, H.-R., Berberich, F. & Graafsma, H. (2003). *Z. Metallkd.* **94**, 1199–1205.

Rietveld, H. M. (1969). *J. Appl. Cryst.* **2**, 65–71.

Trueman, C. N. G., Behrensmeyer, A. K., Tuross, N. & Weiner, S. (2004). *J. Arch. Sci.* **31**, 721–739.

Weiner, S. & Price, P. A. (1986). *Calcif. Tissue Res.* **39**, 365–375.

Wenk, H.-R. & Heidelbach, F. (1998). *Bone*, **24**, 361–369.

Wenk, H.-R. & Grigull, S. (2003). *J. Appl. Cryst.* **36**, 1040–1049.

Wenk, H.-R., Lonardelli, I., Pehl, J., Devine, J., Prakapenka, V., Shen, G. & Mao, H.-K. (2004). *Earth Planet. Sci. Lett.* **226**, 507–519.

Wenk, H.-R., Matthies, S., Donovan, J. & Chateigner, D. (1998). *J. Appl. Cryst.* **31**, 262–269.

Wheeler, E. J. & Leweis, D. (1977). *Calcif. Tissue Res.* **24**, 243–251.

Xie, Y., Wenk, H.-R. & Matthies, S. (2003). *Tectonophysics*, **370**, 269–286.

Ziv, V. & Weiner, S. (1993). *Connect. Tissue Res.* **29**, 1–11.